Received 6 May 2023; revised 14 June 2023; accepted 18 June 2023. Date of publication 5 July 2023; date of current version 21 July 2023.

Digital Object Identifier 10.1109/OJAP.2023.3292390

A Dual Wide-Band Mushroom-Shaped Dielectric Antenna for 5G Sub-6-GHz and mm-Wave Bands

REZA SHAMSAEE MALFAJANI [1] (Graduate Student Member, IEEE), HAMED NIKNAM [2], SAMPADA BODKHE [2], DANIEL THERRIAULT [2], JEAN-JACQUES LAURIN [1] (Senior Member, IEEE), AND MOHAMMAD S. SHARAWI [1] (Senior Member, IEEE)

[1]Department of Electrical Engineering, Polytechnique Montreal, Montreal, QC H3T 1J4, Canada

[2]Department of Mechanical Engineering, Polytechnique Montreal, Montreal, QC H3T 1J4, Canada

CORRESPONDING AUTHOR: R. SHAMSAEE MALFAJANI (e-mail: r.shamsaee@polymtl.ca)

This work was supported by the Fonds de recherche du Québec Nature et technologies (FRQNT) under Grant 2022-PR-298793. The work of Reza Shamsaee Malfajani was supported by de bourses d'excellence pour étudiants étrangers (PBEEE) Doctoral Research Awards (V1). The work of Hamed Niknam was supported by de bourses de recherche du Québec Nature et technologies (FRQNT) Postdoctoral Awards (B3X).

ABSTRACT The design and implementation of a dual wide-band mushroom-shaped antenna are presented in this paper. The antenna consists of a cylindrical dielectric resonator (cDRA), a cylindrical dielectric rod as a waveguide (cDR), and a dielectric lens (DL). The cDRA in conjunction with the DL acts as a sub-6-GHz antenna. At the mm-wave band, the small cDR acts as a waveguide, which transfers the wave from the feed toward the larger cDRA and the DL in order to produce a high gain. A dual wide-band antenna is designed and fabricated with different dielectric constants for the cDRA/cDR and the DL. 3D printing is utilized to precisely control the dielectric constant of printed component. Measurement results show a maximum gain of 6.4 dB at 5.3 GHz with a 21% 3-dB gain bandwidth and 12.7 dB at 31.5 GHz with a 26.2% 3-dB gain bandwidth. The sub-6-GHz band exhibits a measured 10-dB return loss bandwidth of 21% (centered at 5.15 GHz), and the mm-wave frequency band demonstrates a measured 10-dB return loss bandwidth of 26.2% (centered at 30.5 GHz).

INDEX TERMS 3D printed antenna, cavity backed, dielectric lens, dielectric resonator antenna, dual-band, wideband antenna.

I. INTRODUCTION

GROWING wireless data traffic requires high-rate data transmission, which necessitates a substantial increase in communication frequencies. This demand has led to the inception of fifth-generation (5G) wireless standards operating at sub-6-GHz and mm-wave band, which provides a 10 to 100 times increase in the data transmission rate. As a result, attempts have been made to develop wideband/multi-band antennas to 5G and beyond for telecommunication systems. Multi-band antennas have various applications in point-to-point and satellite communication systems. Moving toward the mm-wave band necessitates the design of high-gain antennas to compensate for signal losses.

DRAs are known for their high efficiency, wide bandwidth, low fabrication cost, and simplicity of excitation. Previous works employed a single DRA element covering several bands close to one another by exploiting special feeding mechanisms and by employing the fundamental and high-order DRA modes [1], [2], [3], [4], [5]. Recently, a high-gain dual-band hemispherical DRA with resonant frequencies of 7.65 and 10.04 GHz has been presented [6]. The antenna is fed by a waveguide. The impedance bandwidth of the antenna is 4.98% and 12.68% at the lower and higher bands, respectively. However, this approach does not apply to 5G in which the frequency bands are far apart.

Dual-band operation with a high-frequency ratio is essential in the new generation of wireless communication systems and various designs have been proposed for that [7], [8], [9], [10]. The approaches mainly rely on employing two distinct elements; one for the lower frequency band and the other for the upper-frequency band [11], [12], [13], [14], [15], [16], [17], [18]. For wide-band operation,

it is necessary to increase the overall size of the antennas. In order to decrease the overall size while maintaining the wide-band operation, a single radiator with two back-to-back folded plates was proposed to design a compact dual-band antenna [19], [20]. This antenna provides bandwidths of 9.7% and 2.1% at center frequencies of 2.4 and 24 GHz (ISM bands), respectively. A dual-band antenna that integrates a microwave hollow DRA with a high-gain mm-wave dielectric Fabry–Perot resonator antenna (FPRA) was proposed in [21]. This design provides a bandwidth of 4.67% at the mm-wave band which is again not sufficient for 5G mm-wave communications. The feed at the mm-wave band is a rectangular metallic waveguide, which is not easy to integrate antenna on RF printed circuit boards. In another study, a microwave DRA and an mm-wave metallic FPRA were integrated to form a dual-band antenna [22]. At the lower band, the antenna exhibits good performance. However, the antenna has a low radiation efficiency at the upper band due to the conductor loss. A large ground plane and conventional feeding for the lower frequency band is used. Most recently, the idea of encapsulated dielectric resonator antennas (E-DRAs) is introduced in [23], which offer efficient performance for dual wideband applications and deliver bandwidths of 33% and 27% centered around frequencies of 3.6 GHz and 30.5 GHz, respectively.

This work presents a novel wideband, high gain, single dielectric antenna element covering two widely separated bands. The design methodology enables the design of a dual-band antenna at the desired frequency ranges. The dielectric antenna used in this work is mushroom-shaped. It consists of a large cDRA on top of a smaller dielectric cylinder acts as a dielectric rod (cDR). In addition, a dielectric lens (DL) is placed on top of the larger DRA. The large dielectric cylinder and the DL serve as a dielectric resonator antenna at sub-6-GHz frequencies. At the mm-wave band, the small cDR acts as a dielectric rod waveguide while the large DR and the DL form a radiating aperture to enhance the gain of the mm-wave signals. Different feeding schemes are utilized at the two bands. A microstrip-fed aperture is used to feed the antenna in the millimeter wave band. At sub-6-GHz, the DRA is fed by a substrate-integrated cavity (SIC) through an annular slot. The same technique has been used in [24] to improve the bandwidth at sub-6-GHz and stabilize the gain patten. However, in contrast to [24], the SIC feed is single-ended in this work (compared to a differential one used before). The antenna presented here is a dual band antenna operating at sub-6-GHz and mm-wave bands but the one in [24] is operating at only sub-6-GHz band. Thus, the contribution in this work is different than that in [24] from an antenna perspective (microwave and mm-wave bands in this work) and the use of the DL.

In this work, fused filament fabrication (FFF) as an additive manufacturing (AM) technology is used to fabricate the proposed design. The major benefits of employing AM are the possibility of fabrication of more complex geometries and reducing the fabrication time [23], [25], [26], [27], [28], [29], [30], [31], [32], [33], [34]. FFF technology has been used to fabricate slot [28], horn [29], patch [30], reflectarray [31], and DRA [23], antennas at microwave and mm-wave bands. In these studies, different type of antennas has been considered with customized filaments, and the effect of 3D printing parameters on the antenna response has been investigated.

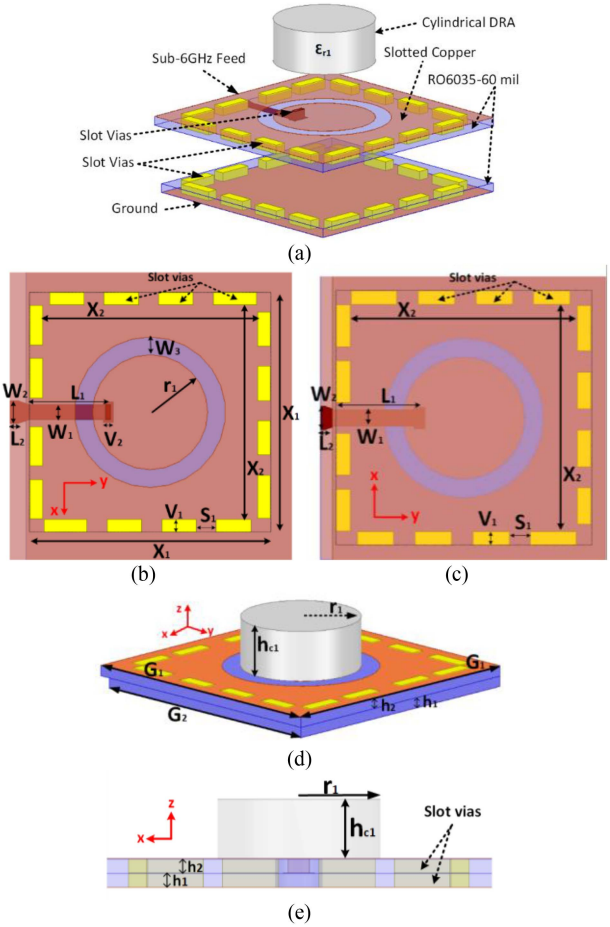

FIGURE 1. Geometry of proposed single feed SIC cDRA (a) Disassembled view (b) Top view (c) Bottom view (d) Perspective view (e) Cross-section from side view.

The remaining sections of this paper are structured as follows. The design of a SIC-backed DRA at sub-6-GHz is described in Section II. In Section III, the designed DRA at sub-6-GHz is modified to act like a lens at mm-wave. A dual-band wide-band mushroom-shaped dielectric antenna is described in Section IV. Characterizations of 3D printing materials and the fabrication process are described in Section V. In Section VI, a detailed analysis of the measurement and simulation results is presented. Finally, a conclusion is drawn in Section VII.

II. DESIGN OF A SIC-BACKED DRA AT SUB-6-GHZ BAND

Figure 1 shows the proposed slot-coupled cDRA backed by an SIC. Compared to simple slot coupling, using a cavity to feed the DRA improves the operating bandwidth and reduces the back lobe of the antenna [24]. For the cDRA designed in this paper, adding the SIC increased the 10-dB return loss bandwidth from 13% to 21%.

The first step in the design process is to choose the appropriate substrate material. Here, Rogers RO3035 with thickness of 1.524 mm is used, which is a low-loss substrate with dielectric constant and loss tangent of 3.5 and 0.0015, respectively. As shown in Fig. 1(a), the cavity consists of two layers of RO3035 substrates, with thicknesses of h_1 and h_2.

Two different techniques are used for DRA fabrication, CNC machining, and 3D printing. For CNC machining, the C-Stock AK material from a Cuming Microwave with a relative permittivity of 10 and loss tangent of 0.002 is used. For 3D Printing the material is PREPERM 3D ABS DK 10.0 with nominal relative permittivity of 10.0 ± 0.35 and loss tangent of 0.003 at 2.4 GHz.

The resonant frequency of the fundamental mode (HEM11δ) for a cDRA can be calculated by [35]:

$$f_{HEM11\delta} = \frac{6.324c_0}{2\pi r\sqrt{\varepsilon_r + 2}}\left(0.27 + 0.36\left(\frac{r_6}{2h}\right) + 0.02\left(\frac{r_6}{2h}\right)^2\right), \quad \left(\text{for } 0.4 \le \frac{r_6}{2h} \le 6\right) \tag{1}$$

where r is the DRA radius, h is the DRA height, and c is the speed of light in free space. The initial value of the radius of the cDRA (r_1) is set equal to one-quarter of the wavelength inside the substrate material at the lowest frequency of the desired band and by using (1), the initial value for the height of cDRA is calculated. For the selected relative permittivity (= 10), the initial values for radius and height of the DRA at 4.6 GHz are selected 6.6 mm and 8.7 mm, respectively. Starting with these initial values, the dimensions are varied to maximize the bandwidth.

A substrate-integrated square cavity specified by the parameters X_1 and X_2 and with a depth of $h_1 + h_2$ is shown in Fig. 1. A short-circuited stripline of length L_1 and width W_1 is printed on the bottom metal layer of the upper substrate. The stripline is shorted with a metallic slot via the top metal layer of the upper substrate of the cavity as shown in Fig. 1(b). The annular slot on the top metal layer of the upper substrate has an inner radius of r_1 and width of W_3. A tapered microstrip line with the length L_2 and width of W_2 is printed on the bottom layer of the top substrate. It is passed through an opening in a sidewall of the cavity and connected to the stripline to feed the antenna at the lower band, as shown in Fig. 1(c).

For the SIC, slot vias were used because of fabrication limitations. Dimensions of the metallic slot vias (V_1 and V_2) and edge-to-edge spacing between them (S_1) are selected based on the fabrication limitations and to ensure that the waves remain confined within the cavity over the operation bandwidth [24]. Initially, the inner dimension of the square cavity (X_1 and X_2) is set to be equal to the one wavelength inside the substrate material at the center frequency of the sub-6-GHz band (5.15 GHz) [36].

In the next step, the DRA dimensions (h_{c1} and r_1) and short-circuited striplines and the annular slot geometrical parameters (W_1, L_1, r_1, W_3) are optimized in ANSYS HFSS to get the best impedance matching over the desired frequency band.

TABLE 1. Final values of the proposed SIC CDRA for sub-6-GHz.

Parameter	Value (mm)	Parameter	Value (mm)
G1	41	r1	8.6
G2	39	hc1	9.3
X1	36.5	W3	2.7
X2	32.5	S1	0.8
h1	1.524	V1	2
h2	1.524	V2	0.8
W1	2.3	L1	11.3
W2	3.4	L2	5.5
hc2	5.9	hc3	7
hL2	4.9	hL3	6.4

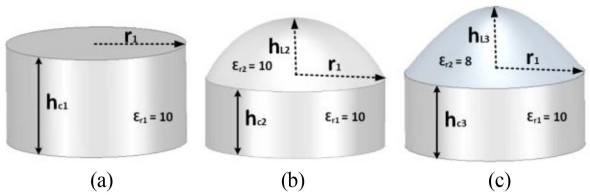

FIGURE 2. Geometry of proposed DRAs (a) CDRA with a single permittivity (b) Lens-shaped DRA with a single permittivity (c) Lens-shaped DRA with two permittivities.

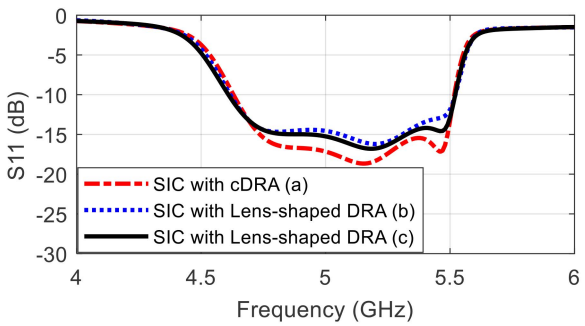

FIGURE 3. Simulated reflection coefficient versus frequency for the different types of DRA shaped antenna with SIC feeding.

The final values of the parameters are listed in Table 1. In this design, a cylindrical dielectric resonator with single permittivity is used as shown in Fig. 2(a). For the same feeding structure and without changing the SIC dimensions, other shapes/materials for the dielectric resonator shown in Fig. 2 provide similar performance. The designs shown in Figs. 2(b) and 2(c) behave like a DL at the mm-wave band. In the design in Fig. 2(b) we used $\varepsilon_{r1} = \varepsilon_{r2} = 10$ and in the design in Fig. 2(c) we used $\varepsilon_{r1} = 10$ and $\varepsilon_{r2} = 8$. The reflection coefficients of the antenna structure with these three DRAs are also shown in Fig. 3, and similar performance can be observed for the sub-6-GHz band. The simulated reflection coefficient of the antenna shows a 10-dB return loss bandwidth of 21% centered at 5.15 GHz. More details on these designs and their performance will be discussed in the next section.

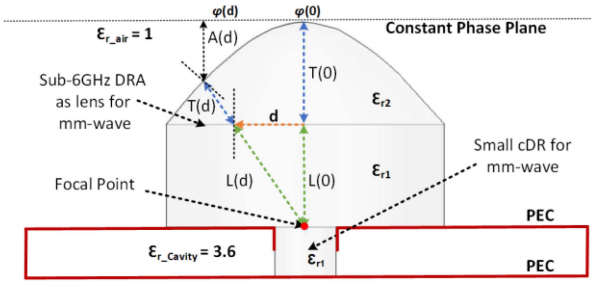

FIGURE 4. Geometry of mushroom-shaped dielectric antenna.

III. MODIFICATION OF THE LOW BAND DRA TO ACT AS A MM-WAVE DL

The DRA used in this work is mushroom-shaped, which consists of a large cDRA on top of a smaller cDR (Fig. 4). A dielectric lens (DL) is placed on top of a large cylinder. The smaller cDR is attached to the bottom of the larger dielectric cylinder, as a part of the feed at the mm-wave band. Both the small cDR and the large cylinder have a relative permittivity of ε_{r1} and the DL has a relative permittivity of ε_{r2}. This mushroom-shaped dielectric is a modified version of the sub-6-GHz structure with the same performance presented in the last section (Fig. 2(a)), that is now able to operate at mm-wave frequencies to improve the gain.

To change the sub-6-GHz DRA in Fig. 2(a) to a DL (Fig. 2(b) or 2(c)) at mm-wave band without any change in the performance at sub-6-GHz band, the profile of the top surface of the lens should be modified. This is done by using a simple ray propagation model. To act like a lens, the fields propagating from the focal point to a plane on top of the lens (Fig. 4) must have the same phase. $T(d)$ defines the profile of the top surface of the lens at the distance of d from the center and $L(d)$ is the distance from the focal point to the interface between the larger cylinder and the bottom surface of the lens. The phase of waves propagating from the focal point to a plane at top of the lens can be described by:

$$\varphi(0) = -k_0\sqrt{\varepsilon_{r1}}L(0) - k_0\sqrt{\varepsilon_{r2}}T(0) \ \text{(for } r = 0) \tag{2}$$

$$\varphi(d) = -k_0\sqrt{\varepsilon_{r1}}L(d) - k_0\sqrt{\varepsilon_{r2}}T(d) - k_0A(d) \ \text{(for } r = d) \tag{3}$$

where k_0 is free-space propagation constant.

Assuming $A(d) \approx T(0) - T(d)$ and a constant phase at a plane at top of the lens, i.e., $\varphi(0) = \varphi(d)$, the profile of the lens can be calculated using as

$$T(d) = \frac{\sqrt{\varepsilon_{r1}}[L(0) - L(d)] + T(0)\left[\sqrt{\varepsilon_{r2}} - 1\right]}{\sqrt{\varepsilon_{r2}} - 1} \tag{4}$$

In (3), $(d) = \sqrt{d^2 + (L(0))^2}$. To reduce the thickness of the lens, it is desired to set $T(d)$ equal to zero when $d = r_1$ so that:

$$\sqrt{\varepsilon_{r1}}[L(0) - L(r_1)] + T(0)\left[\sqrt{\varepsilon_{r2}} - 1\right] = 0 \tag{5}$$

This provides the maximum thickness $(T(0))$ of the top part of the DL:

$$T(0) = \frac{\sqrt{\varepsilon_{r1}}\left[\sqrt{(r_1)^2 + (L(0))^2} - L(0)\right]}{\sqrt{\varepsilon_{r2}} - 1} \tag{6}$$

Hence, the profile of the top surface of the dielectric lens is calculated based on its permittivity, r_1, and the focal length $(L(0))$. Given the approximation on $A(d)$ above, $T(d)$ does not accurately represent the DL profile but it can provide a good estimation of that to find the initial values for the dimensions of the DL for further optimizations. Initially, the focal point is placed at the top of the small cDR (aperture of the waveguide). hc3 is the height of the cylindrical part of the DRA and L(0) is the focal length for the dielectric lens which is not qual to hc3 in general. Since the focal point of the dielectric lens antenna is not known from the beginning, the initial value for focal length is approximately h_{c3}. The initial value for focal length should be optimized based on the shape of patterns at different frequencies within the mm-wave band.

IV. DESIGN OF THE DUAL-BAND DIELECTRIC ANTENNA

In this section, the cavity is modified to accept the mushroom-shaped dielectric antenna. The disassembled view of the mushroom-shaped antenna and the modified cavity are shown in Fig. 5(a). The modified cavity has a hole at the center to feed the antenna at the mm-wave band through a slot, as shown in Fig. 5(c). The cavity feeds the antenna at the sub-6-GHz band as discussed in Section II. The mm-wave feeding slot is at the center of the ground layer and its dimensions are specified by L_s, and W_s, as shown in Fig. 5(c). A 50-Ω microstrip line with a width of W_4 and length of L_3 is used to feed the slot. The small dielectric cylinder (or rod) acts as a waveguide. The height of the cavity is fixed based on substrate selection for the sub-6-GHz band (h_1+h_2). As can be observed in Fig. 5a, the hole where the dielectric rod is placed is only plated in the top substrate. Based on the simulations, such plating results in a better side lobe level at mm-wave bands. So, the upper part of the rod forms a circular metallic waveguide filled with the dielectric. The minimum diameter for the dielectric rod is determined by the cut-off frequency of this guide. With the selected diameter, the cut-off frequency is about 15 GHz which is well below the desired mm-wave band of operation of the antenna. The bottom part of the rod embedded in the lower substrate forms a dielectric guide with no (i.e., zero) cut-off frequency.

In the next step, the mm-wave feed dimensions (W_s, L_s, L_3, r_2, and r_3) are optimized to obtain the best matching over the mm-wave band. Figure 6 displays the antenna's reflection coefficient as a function of frequency within the mm-wave band, with various values of W_s, L_s, r_2 and r_3 while keeping other design parameters fixed at the values listed in Table 2.

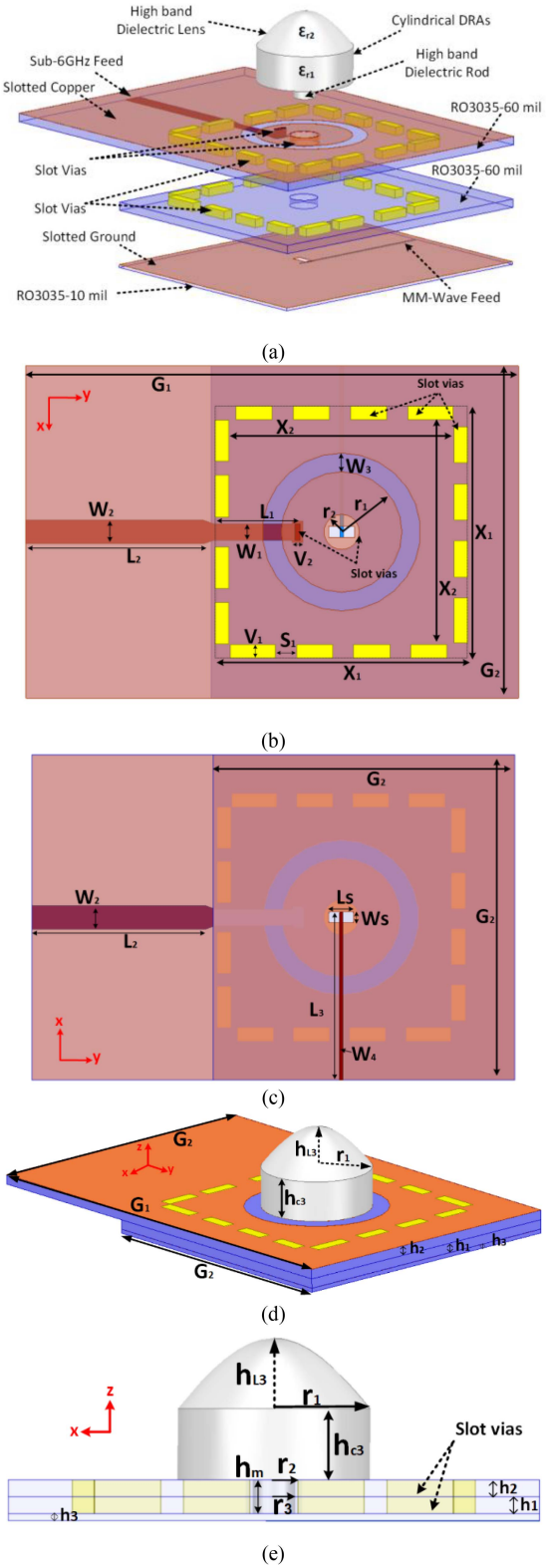

FIGURE 5. Geometry of proposed mushroom-shaped DRA (a) Disassembled view (b) Top view (c) Bottom view (d) Perspective view (e) Cross-section from side view.

In the next step, the cavity with the small dielectric rod at the center is fine-tuned around the geometrical values provided in Section II. Figure 7 shows the reflection coefficient

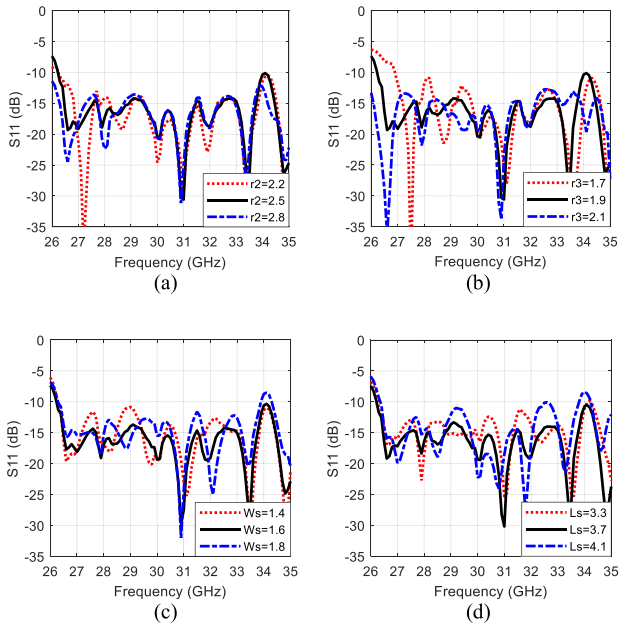

FIGURE 6. Reflection coefficient of the antenna at mm-wave band versus frequency for different values (a) r_2, (b) r_3, (c) W_s, and (d) L_s.

TABLE 2. Final values of the proposed dual band mushroom-shaped dielectric antenna.

Parameter	Value (mm)	Parameter	Value (mm)
G1	75	r1	8.6 (11.8)
G2	42	hc3	6.4 (7.2)
X1	36.5 (48.5)	W3	2.9 (2.4)
X2	32.5 (44.5)	S1	0.8
h1	1.524	V1	2
h2	1.524	V2	0.8
h3	0.254	hL3	6.4 (8.8)
W1	2.3	L1	10.8 (15.6)
W2	3.4	L2	29.6 (7.6)
Ws	1.6	Ls	3.7
r3	1.9	hm	3.08
W4	0.56	L3	9.3
r2	2.53	hm	h1+h2

of the antenna versus frequency for different values of L_1, r_1, h_{c3}, and X_2 at the sub-6-GHz band. These results are for a mushroom-shaped DRA with $\varepsilon_{r1} = 10$ and $= \varepsilon_{r2} = 8$. Other parameters are set according to the values shown in Table 2. In that Table 2, parameter values in parenthesis are for another design of the sub-6-GHz antenna, covering the 3.5-4 GHz band. This illustrates the capability of this design to cover different bands of the 5G sub-6 spectrum.

In the next step, optimization is done for the top profile of the lens at the mm-wave frequency to get the best radiation characteristics and matching. As shown in Fig. 8b, the lowest side lobe level (SLL) is obtained when $L(0) =$ 11.4 mm. By changing the L(0), only the profile of the top surface of the dielectric lens will be changed and h_{c3} is fix. Fig. 8(c) and (d) also show that varying this parameter has no significant effect on sub-6-GHz performance.

To reduce the reflection from the lens-air interface, it is better to select a smaller dielectric constant for the top curved

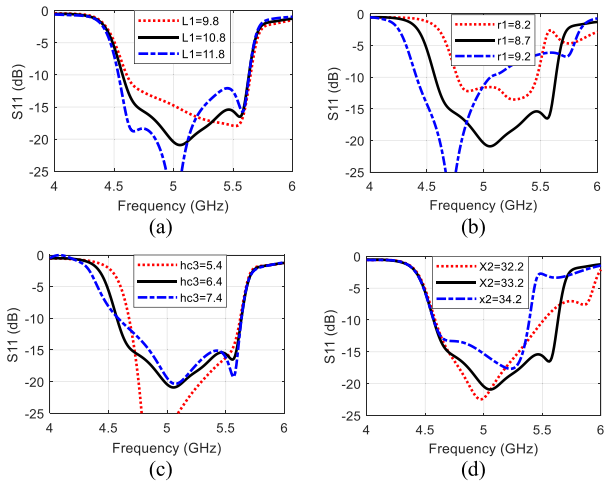

FIGURE 7. Reflection coefficient of the antenna at sub-6-GHz band versus frequency for different values (a) L_1 (b) r_1, (c) h_{c3}, and (d) X_2.

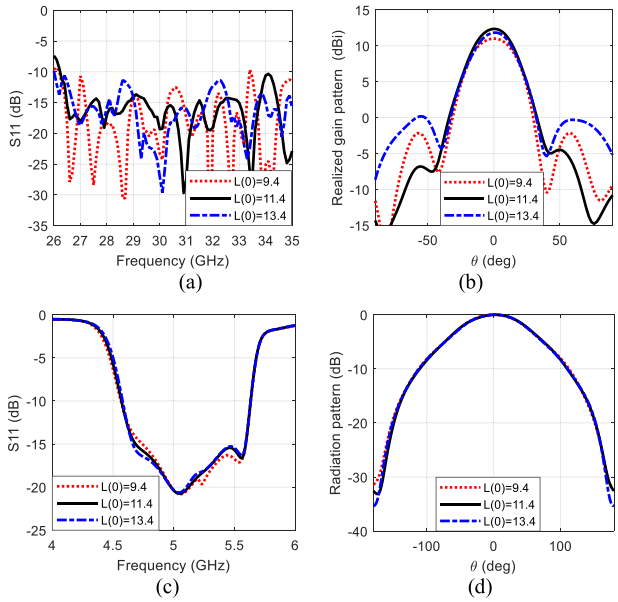

FIGURE 8. (a) Reflection coefficient of the antenna at mm-wave band versus frequency for different values L(0), and (b) H-plane realized gain pattern at 30 *GHz*, (c) Reflection coefficient of the antenna at sub-6-GHz versus frequency for different values L(0), and (d) normalized radiation pattern at 5.15 GHz.

part of the lens, so the value 8 or smaller is better than 10 for the lens performance. In addition, in this design, since the dielectric constant of the top part of the DL and the larger cylindrical dielectric (bottom part of DL) are very close (i.e., 8 and 10, respectively), the reflection from their interface is negligible. Fig. 9 presents the effect of varying ε_{r2} based on equations (4) and (6) at the mm-wave band. It can be observed that the gain/pattern/SLL is better when the top part of DL is made of a material with a relative permittivity of 8 as compared to the case where DL is completely made of a material with a relative permittivity of 10. For the four values of permittivity shown in Figure 9, the lens profile was re-optimized based on equations (4) and (6). The optimum

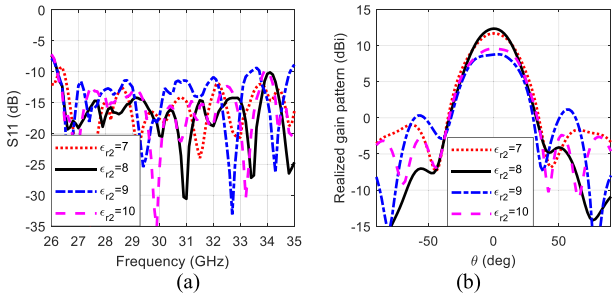

FIGURE 9. (a) Reflection coefficient of the antenna at mm-wave band versus frequency for different values ε_{r2}, and (b) H-plane realized gain pattern at 30 GHz.

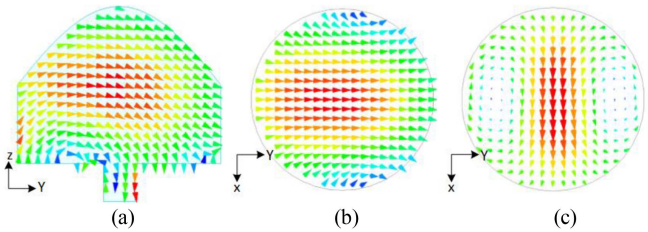

FIGURE 10. Field distributions in the mushroom-shaped DRA at center frequency (5.15 GHz) (a) Side view of the electric field, (b) Top view of the electric field, and (c) Top view of the magnetic field.

geometrical parameter values based on the simulation results are listed in Table 2.

The antenna design presented in this study offers versatility for various applications that demand an impedance bandwidth exceeding 20% in both sub-6-GHz and mm-wave frequency bands, exemplified by the proof-of-concept 5G antenna capable of supporting sub-6-GHz bands such as n46/n79 and mm-wave bands such as n257/n261 [23]. For the design of the antenna at a lower frequency band at sub-6-GHz, the size of the cavity and the larger cDRA must be increased.

The electric and magnetic field distributions inside the sub-6-GHz DRA at center frequency are shown in Fig. 10. The principal mode in the DRA is $\text{HEM}_{11\delta}$ based on the presented field distributions, which provides broadside radiation. This field distribution is not perfectly symmetric due to unbalanced feeding, but it still provides a broadside radiation pattern. As shown in [24], by feeding the DRA using an SIC, the DRA over the desired sub-6-GHz band has a single-mode operation. The E-field magnitude inside the mushroom-shaped antenna at the center frequency of the mm-wave band is shown in Fig. 11(a). It can be seen that the beam is collimated toward the z-axis which indicates improved radiation gain at broadside direction. Fig. 11(b) shows the phase of the electric field inside the mushroom-shaped antenna at the same frequency. It can be observed that a flat wavefront is achieved in the "constant phase plane" defined in Fig. 4.

V. FABRICATION OF THE MUSHROOM-SHAPED DRA

The mushroom-shaped part of the proposed design has two different relative permittivities of 10 and 8. The small and

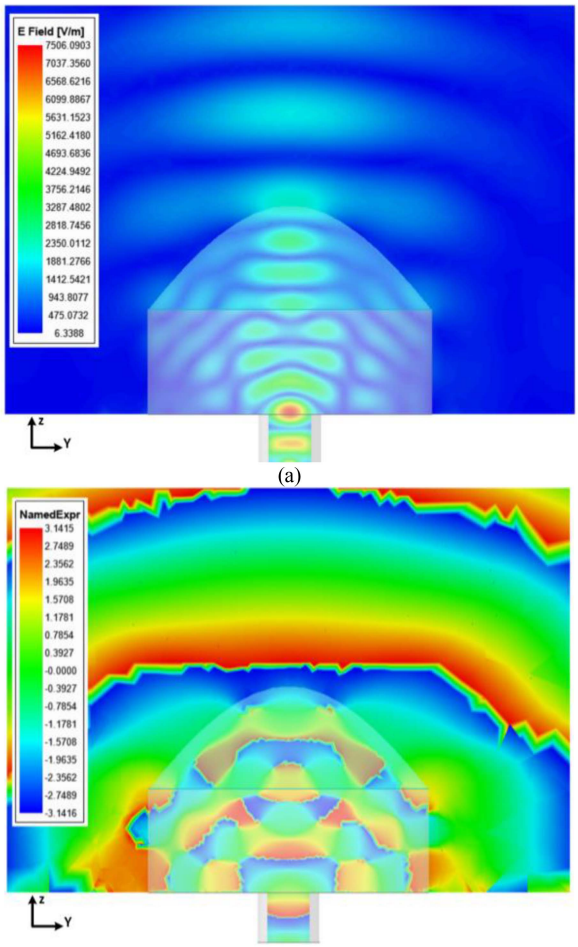

FIGURE 11. (a) The magnitude of the electric field of the mushroom DRA at 30.5 GHz. (b) The phase of the electric field of the mushroom DRA at 30.5 GHz.

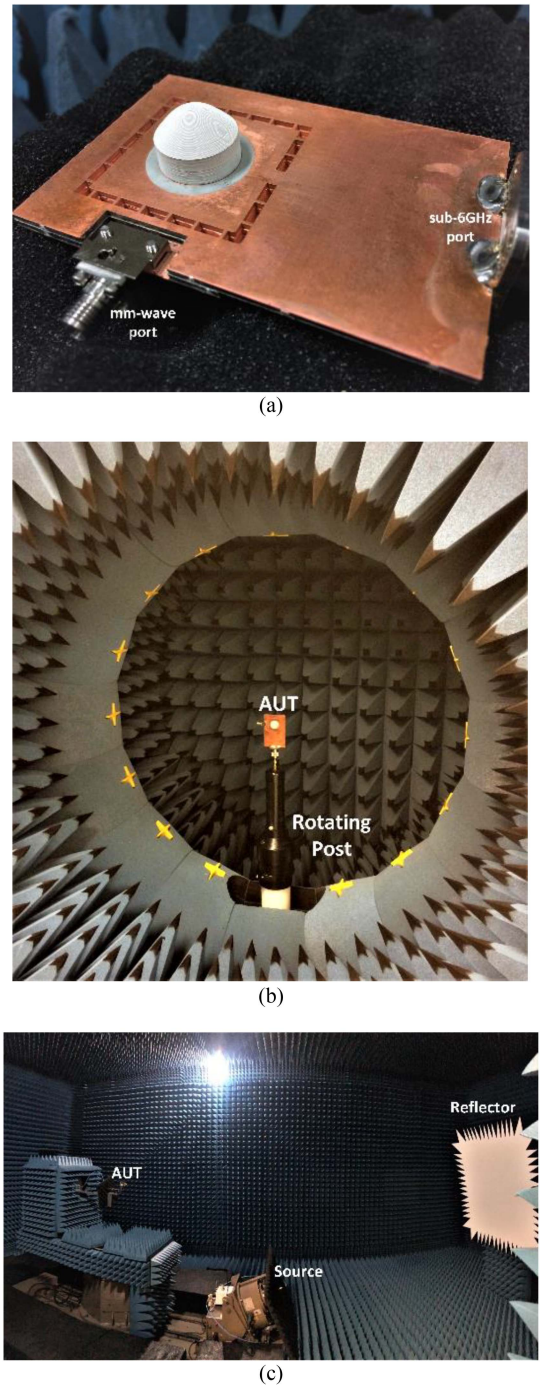

FIGURE 12. (a) Photograph of the fabricated DRA. (b) Measurement setup for sub-6-GHz (c) Measurement setup for mm-wave.

the large cylindrical dielectrics are fabricated by machining a slab of the C-Stock AK from Cuming Microwave.

The top-shaped dielectric part is 3D printed utilizing FFF technology which is an extrusion-based additive manufacturing technology. In FFT, a polymer-based filament is fed into an extruding nozzle and then the filament is melted and extruded based on the input geometry and deposited layer by layer.

Based on the required relative permittivity (8), commercial PREPERM ABS1000® material is used for fabrication, which is a special compound based on Premix proprietary ABS technology. The nominal relative permittivity of the material is 10 and it is stable over a wide range of frequencies and temperatures, with a low loss tangent of 0.003.

3D printing enables tuning the permittivity of the fabricated part by controlling the infill percentage. The actual relative permittivity of printed parts is found to be less than the nominal relative permittivity of the filaments even for the 100 percent infill. This is because of the presence of voids [23], [32], [37]. Previous studies show that Bruggeman's model [38] can approximate the relative permittivity of 3D printed samples with an acceptable accuracy [23], [37]. Here, the same model is adopted to estimate the infill percentage needed to obtain the desired permittivity.

The print settings and parameters are selected according to the filament manufacturer instructions and to achieve the highest quality samples with minimum defects. A summary of the AM parameters and settings for printing are listed in Table 3. The extrusion temperature is 20°C higher than the temperature recommended by the filament manufacturer in order to achieve a higher surface quality. Also, a concentric

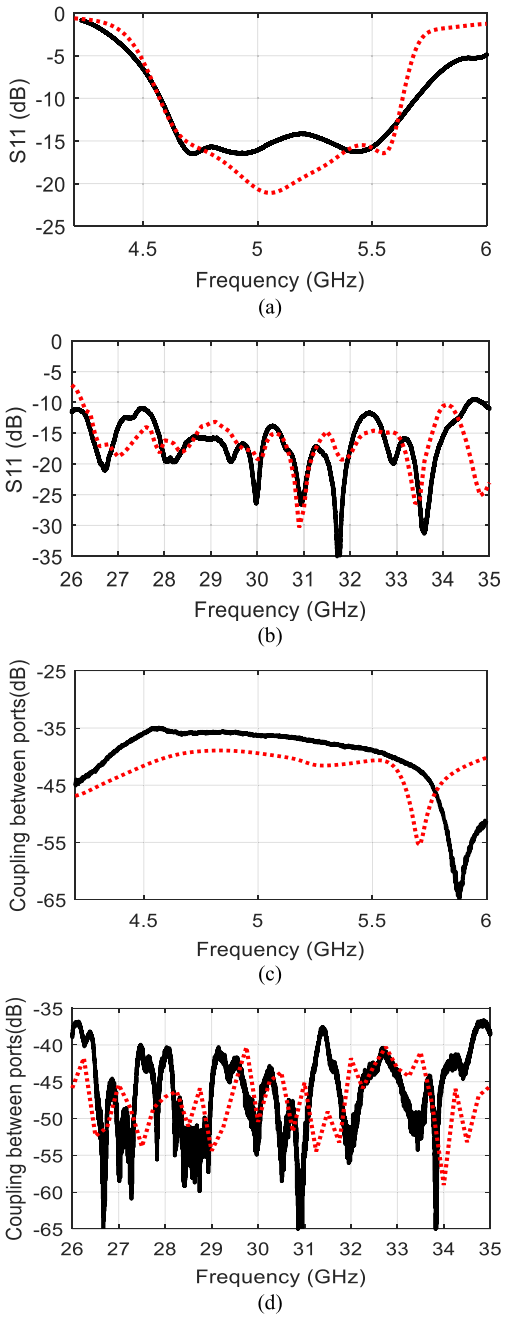

FIGURE 13. Measured (solid line) and simulated (dashed line) reflection coefficient of the proposed antenna at (a) Sub-6-GHz band, (b) mm-wave band, and (c) isolation between two ports.

infill pattern is selected mainly to avoid any anisotropic dielectric properties in the samples.

VI. SIMULATION AND MEASUREMENT RESULTS FOR THE FABRICATED ANTENNA

The designed dual-band mushroom-shaped DRA was simulated at both sub-6-GHz and mm-wave frequency bands in ANSYS HFSS and the results are presented in this section. The dimensions of the fabricated antenna are presented in Table 2. Fig. 12 presents the image of the fabricated antenna

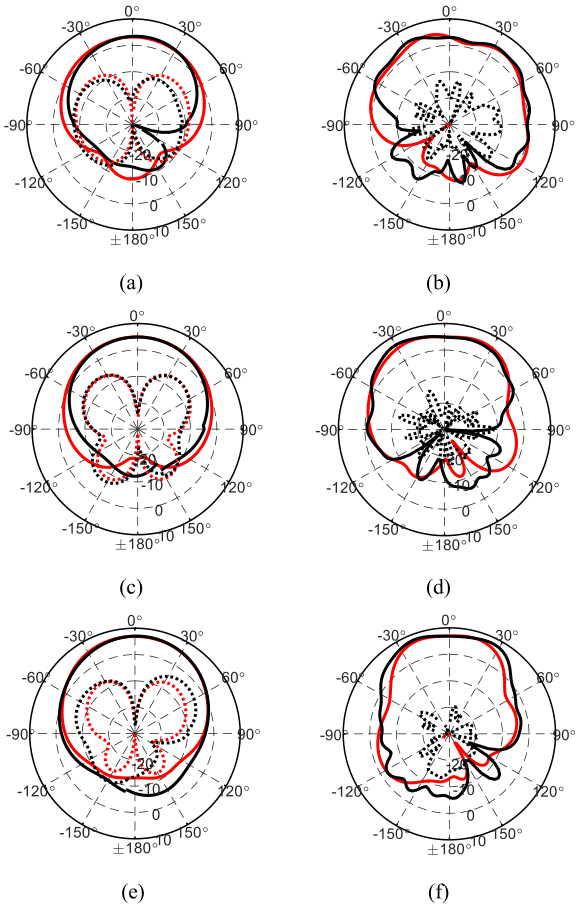

FIGURE 14. Measured (black line) and simulated (red line) co/cross (solid line) /(dashed line) polarization radiation patterns for the proposed antenna: (a) 4.6 GHz at H-plane, (b) 4.6 GHz at E-plane, (c) 5.15 GHz at H-plane, (d) 5.15 GHz at E-plane, (e) 5.7 GHz at H-plane, (f) 5.7 GHz at E-plane.

TABLE 3. AM parameters and settings for printing lens-shaped DRA.

Extrusion temperature (°C)	Printing speed (mm/s)	Infill pattern	Layer height (mm)	Nozzle diameter (mm)
265	30	Concentric	0.1	0.4

and the measurement setups. Fig. 13 shows the measured and simulated reflection coefficients of the antenna. The simulation and measurement results indicate a significant level of agreement. For the sub-6-GHz band, the measured −10 dB reflection coefficient bandwidth is 21%, centered at 5.15 GHz. Similarly, for the mm-wave band, the measured −10 dB reflection coefficient bandwidth is 26.5%, centered at 30.5 GHz. The isolation between the two antenna ports (each is used for one band) is better than 35 dB and 37 dB in sub-6-GHz and mm-wave bands, respectively, as can be seen in Fig. 13(c) and (d).

According to Fig. 5, the polarization at both bands is linear with the direction along x at sub-6-GHz and along y at the mm-wave band. In Fig. 14, the radiation patterns of the antenna at 4.6 GHz, 5.15 GHz, and 5.7 GHz for

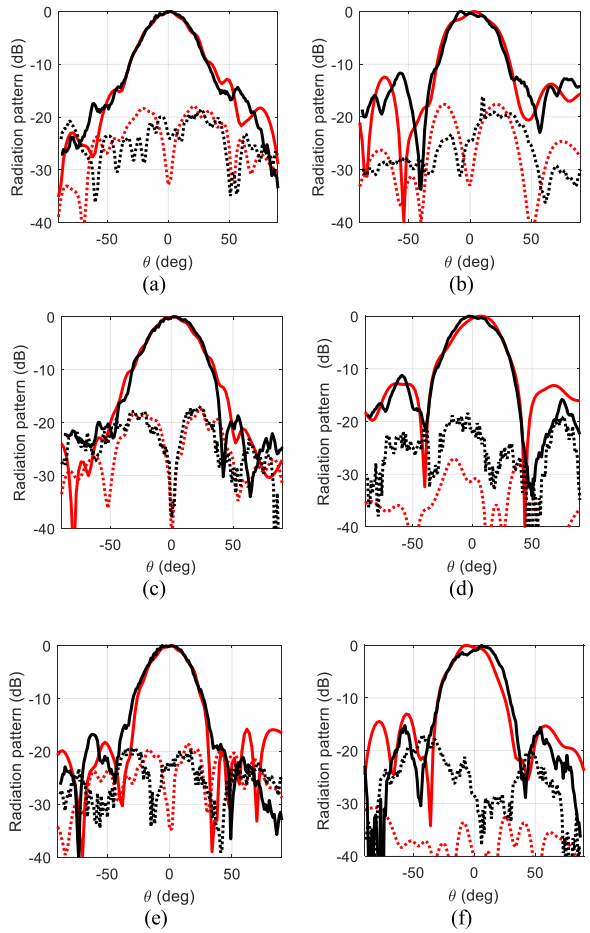

FIGURE 15. Measured (black line) and simulated (red line) co/cross (solid line) /(dashed line) polarization radiation patterns for the proposed antenna: (a) 28 GHz at H-plane, (b) 28 GHz at E-plane, (c) 30.5 GHz at H-plane, (d) 30.5 GHz at E-plane, d) 33 GHz at H-plane, and (b) 33 GHz at E-plane.

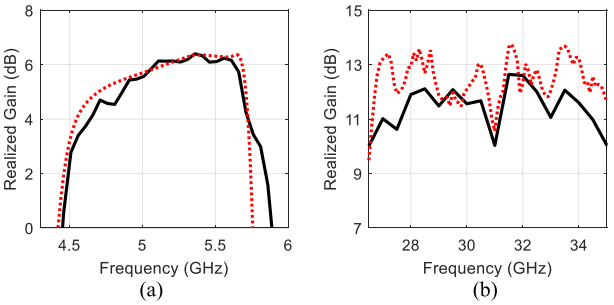

FIGURE 16. Measured and simulated realized gain at (a) Sub-6-GHz and (b) mm-wave band. (Measured results are in solid lines, whereas simulated ones are in dashed lines).

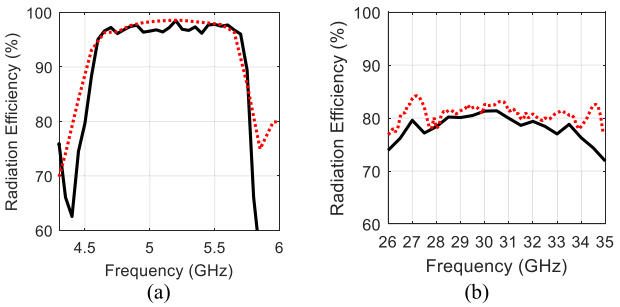

FIGURE 17. Measured and simulated radiation efficiency at (a) Sub-6-GHz and (b) mm-wave band. (Measured results are in solid lines, whereas simulated ones are in dashed lines).

sub-6-GHz are presented. The results of simulation and measurement for co/cross-polarization E- and H-plane radiation patterns (normalized to the maximum of the co-polarization) at 28, 30.5 and 33 GHz are presented in Fig. 15. The results obtained from measurements and simulations exhibit a high level of agreement. The SLL achieves values lower than −12 dB and −15 dB in the E-plane and H-plane, respectively, while the cross-polarization level remains below −20 dB in the broadside direction. The main result for the difference between simulation and measurement is degradation in cross-polarization levels in the experimental results, which is possibly due to misalignment.

The measured and simulated realized gain versus frequency at sub-6-GHz and mm-wave bands of the antenna are shown in Fig. 16. According to Fig. 16(a), at sub-6-GHz band, the maximum gain is 6.4 dBi at 5.3 GHz. The measured 1-dB and 3-dB gain relative bandwidths are 15% and 21%. According to Fig. 16(b), at the mm-wave band, the maximum gain is 12.7 dBi (at 31.5 GHz) and the measured 3-dB gain relative bandwidths are 26.2%.

Fig. 17 shows the radiation efficiency at the antenna in both bands. In this figure, the radiation efficiency is measured by Satimo Starlab near-field chamber for sub-6-GHz. The radiation efficiency is calculated by dividing the measured realized gain by the simulated directivity [39] for the mm-wave band. The minimum total efficiency is 95% over the sub-6-GHz band and 77% over the mm-wave band. A comparison of the measured performance of the proposed antenna with the previous works on dual-band DRAs is given in Table 4.

The idea behind the proposed antenna was to use a new feeding technique for the dual-band dielectric antenna at both sub-6GHz and mm-wave frequency bands. The DRA was modified as an mm-wave lens without changing its size, resulting in high gain and wideband antenna performance at mm-wave frequency. According to Table 4, the proposed antenna has a smaller size compared to [5], [6], [21], and [22]. Tough [17] has a smaller size, and its impedance bandwidth is much less than that of the proposed antenna. Compared to other works, the proposed antenna achieved the most significant wide bandwidth at mm-wave frequency and high bandwidth for the lower frequency band. The antenna is made of low-loss dielectric materials for both bands and thus exhibits a high radiation efficiency in both bands. The main part of the antenna (the inner part of the cavity) has a lateral size of 32.5 mm x 32.5 mm (Table 4).

VII. CONCLUSION

A novel dual wide-band mushroom-shaped antenna has been proposed for operation at sub-6-GHz and mm-wave

TABLE 4. Comparison of the measured performance of proposed DRA with the previous works on dual band DRAs.

Reference	This work	[22]	[21]	[17]	[6]	[5]
Center Frequency (GHz)	**5.15/30.5**	2.72/25.3	2.73/24.4	5.2/24	7.65/10.04	3.5/10.25
Frequency Ratio	**5.92**	9.3	8.93	4.61	1.31	2.92
Measured BW (|S11|<-10 dB) %	**21/26.2**	38.2/16.2	30.8/4.7	1.93/3.21	4.98/12.7	40.2/19.5
Max. Measured Gain (dBi)	**6.4/12.7**	6.5/11.3	8.23/17.2	3.9/6.3	11.72/11.5	5.8/12
Polarization	**Orthogonal LP**	Orthogonal LP	Single LP	Orthogonal LP	Single LP	Single LP
Antenna type (Ssub-6-GHz/mm-wave)	**DRA/DL**	DRA/FPRA	DRA/FPRA	Slot/SIDRA	DRA/DRA	DRA/DL
Antenna Size (*/λ_0^3)	$\mathbf{0.72 \times 1.28 \times 0.27}$** $\mathbf{0.72 \times 0.72 \times 0.27}$***	$1.36 \times 1.36 \times 0.34$	$\sim 1.31 \times 1.31 \times 0.31$	$0.69 \times 0.43 \times 0.03$	$2.55 \times 2.55 \times 1.92$	$0.7 \times 0.82 \times 0.34$
DR Size (*/λ_0^3)	$\boldsymbol{\pi \times 0.14^2 \times 0.27}$	$0.2 \times 0.23 \times 0.31$	$\pi \times 0.21^2 \times 0.18$	$\pi \times 0.06^2 \times 0.03$	$\pi \times 1.17^2 \times 0.36$	$\pi \times 0.16^2 \times 0.34$
Min. Antenna Efficiency (%)	**95/77**	75/57	84.1/80	38/-	99/99	86/85
Capability for integrated with PCB boards	**Yes**	No	No	Yes	No	Yes

*λ_0 is the free-space wavelength at the center frequency of low band.
**antenna overall size including extended feed line for sub-6-GHz (the extended feed line is required to connect an N-type connector).
***antenna size without extended feed line for sub-6-GHz.

frequency bands with a high-frequency ratio. For improving the bandwidth at sub-6-GHz, a cavity is used to feed the DRA. The cavity supports two modes to provide almost the same excitation for the DRA over a wide bandwidth resulting in a stable radiation characteristic for the antenna. The sub-6-GHz DRA also acts as a dielectric lens at the mm-wave and so improves the gain at the mm-wave band. The measurement results show the maximum gain of 6.4 dBi at sub-6-GHz and 12.7 dBi at mm-wave. The proposed antenna shows more than 20% 10-dB impedance bandwidth at both sub-6-GHz and mm-wave bands. In the fabrication of the antenna, a 3D printing technique has been used which enabled control of the dielectric constant and shape of the fabricated lens.

REFERENCES

[1] P. Kumar et al., "Electronically controlled beam steerable dual-band star-shaped DRA for UAS and Wi-Fi data link applications," *IEEE Trans. Antennas Propag.*, vol. 68, no. 10, pp. 7214–7218, Oct. 2020.
[2] S. Mishra et al., "Three-dimensional dual-band dielectric resonator antenna for wireless communication," *IEEE Access*, vol. 8, pp. 71593–71604, 2020.
[3] H. Tang, J.-X. Chen, W.-W. Yang, L.-H. Zhou, and W. Li, "Differential dual-band dual-polarized dielectric resonator antenna," *IEEE Trans. Antennas Propag.*, vol. 65, no. 2, pp. 855–860, Feb. 2017.
[4] X.-C. Wang, L. Sun, X.-L. Lu, S. Liang, and W.-Z. Lu, "Single-feed dual-band circularly polarized dielectric resonator antenna for CNSS applications," *IEEE Trans. Antennas Propag.*, vol. 65, no. 8, pp. 4283–4287, Aug. 2017.
[5] Z.-X. Xia, K. W. Leung, P. Gu, and R. Chen, "3-D-printed wideband high-efficiency dual-frequency antenna for vehicular communications," *IEEE Trans. Veh. Technol.*, vol. 71, no. 4, pp. 3457–3469, Apr. 2022.
[6] S. Varghese, P. Abdulla, A. M. Baby, and P. M. Jasmine, "High-gain dual-band waveguide-fed dielectric resonator antenna," *IEEE Antennas Wireless Propag. Lett.*, vol. 21, no. 2, pp. 232–236, Feb. 2022.
[7] X.-H. Ding, W.-W. Yang, W. Qin, and J.-X. Chen, "A broadside shared aperture antenna for (3.5, 26) GHz mobile terminals with steerable beam in millimeter-waveband," *IEEE Trans. Antennas Propag.*, vol. 70, no. 3, pp. 1806–1815, Mar. 2022.
[8] T. Li and Z. N. Chen, "Shared-surface dual-band antenna for 5G applications," *IEEE Trans. Antennas Propag.*, vol. 68, no. 2, pp. 1128–1133, Feb. 2020.
[9] Y. Su, X. Q. Lin, and Y. Fan, "Dual-band coaperture antenna based on a single-layer mode composite transmission line," *IEEE Trans. Antennas Propag.*, vol. 67, no. 7, pp. 4825–4829, Jul. 2019.
[10] J. F. Zhang, Y. J. Cheng, Y. R. Ding, and C. X. Bai, "A dual-band shared-aperture antenna with large frequency ratio, high aperture reuse efficiency, and high channel isolation," *IEEE Trans. Antennas Propag.*, vol. 67, no. 2, pp. 853–860, Feb. 2019.
[11] T. Zhihong, Y. P. Zhang, C. Luxey, A. Bisognin, D. Titz, and F. Ferrero, "A ceramic antenna for tri-band radio devices," *IEEE Trans. Antennas Propag.*, vol. 61, no. 11, pp. 5776–5780, Nov. 2013.
[12] L. Zhang, K. Y. See, B. Zhang, and Y. P. Zhang, "Integration of dual-band monopole and microstrip grid array for single-chip tri-band application," *IEEE Trans. Antennas Propag.*, vol. 61, no. 1, pp. 439–443, Jan. 2013.
[13] Z.-X. Xia, K. W. Leung, N. Yang, and K. Lu, "Compact dual-frequency antenna array with large frequency ratio," *IEEE Trans. Antennas Propag.*, vol. 69, no. 4, pp. 2031–2040, Apr. 2021.
[14] T. Smith, U. Gothelf, O. S. Kim, and O. Breinbjerg, "An FSS-backed 20/30 GHz circularly polarized reflectarray for a shared aperture L- and Ka-band satellite communication antenna," *IEEE Trans. Antennas Propag.*, vol. 62, no. 2, pp. 661–668, Feb. 2014.
[15] T. Li, and Z. N. Chen, "Metasurface-based shared-aperture 5G ${S}$ -/ ${K}$ -band antenna using characteristic mode analysis," *IEEE Trans. Antennas Propag.*, vol. 66, no. 12, pp. 6742–6750, Dec. 2018.
[16] Y. R. Ding and Y. J. Cheng, "Ku/Ka dual-band dual-polarized shared-aperture beam-scanning antenna array with high isolation," *IEEE Trans. Antennas Propag.*, vol. 67, no. 4, pp. 2413–2422, Apr. 2019.
[17] Y.-X. Sun and K. W. Leung, "Substrate-integrated two-port dual-frequency antenna," *IEEE Trans. Antennas Propag.*, vol. 64, no. 8, pp. 3692–3697, Aug. 2016.
[18] W.-W. Yang, X.-H. Ding, T.-W. Chen, L. Guo, W. Qin, and J.-X. Chen, "A shared-aperture antenna for (3.5, 28) GHz terminals with end-fire and broadside steerable beams in millimeter wave band," *IEEE Trans. Antennas Propag.*, vol. 70, no. 10, pp. 9101–9111, Oct. 2022.
[19] L. Y. Feng and K. W. Leung, "Dual-frequency folded-parallel-plate antenna with large frequency ratio," *IEEE Trans. Antennas Propag.*, vol. 64, no. 1, pp. 340–345, Jan. 2016.
[20] K. Lu, Y. Ding, and K. W. Leung, "A new Fabry–Perot resonator antenna fed by an L-probe," *IEEE Trans. Antennas Propag.*, vol. 60, no. 3, pp. 1237–1244, Mar. 2012.
[21] L. Y. Feng and K. W. Leung, "Dual-fed hollow dielectric antenna for dual-frequency operation with large frequency ratio," *IEEE Trans. Antennas Propag.*, vol. 65, no. 6, pp. 3308–3313, Jun. 2017.
[22] L. Y. Feng and K. W. Leung, "Wideband dual-frequency antenna with large frequency ratio," *IEEE Trans. Antennas Propag.*, vol. 67, no. 3, pp. 1981–1986, Mar. 2019.

[23] R. S. Malfajani, H. Niknam, S. Bodkhe, D. Therriault, J.-J. Laurin, and M. S. Sharawi, "A 3D-printed encapsulated dual wide-band dielectric resonator antenna with beam switching capability," *IEEE Open J. Antennas Propag.*, vol. 4, pp. 492–505, 2023.
[24] R. S. Malfajani, J.-J. Laurin, and M. S. Sharawi, "Wideband substrate integrated cavity-backed dielectric resonator antenna at sub-6-GHz band," *IEEE Open J. Antennas Propag.*, vol. 4, pp. 60–68, 2023.
[25] F. Calignano et al., "Overview on additive manufacturing technologies," *Proc. IEEE*, vol. 105, no. 4, pp. 593–612, Apr. 2017.
[26] A. I. Dimitriadis et al., "Polymer-based additive manufacturing of high-performance waveguide and antenna components," *Proc. IEEE*, vol. 105, no. 4, pp. 668–676, Apr. 2017.
[27] B. Zhang, Y.-X. Guo, H. Zirath, and Y. P. Zhang, "Investigation on 3-D-printing technologies for millimeter-wave and terahertz applications," *Proc. IEEE*, vol. 105, no. 4, pp. 723–736, Apr. 2017.
[28] S. Alkaraki et al., "Compact and low-cost 3-D printed antennas metalized using spray-coating technology for 5G mm-Wave communication systems," *IEEE Antennas Wireless Propag. Lett.*, vol. 17, no. 11, pp. 2051–2055, Nov. 2018.
[29] G. Addamo et al., "3-D printing of high-performance feed horns from Ku- to V-bands," *IEEE Antennas Wireless Propag. Lett.*, vol. 17, no. 11, pp. 2036–2040, Nov. 2018.
[30] M. Liang, C. Shemelya, E. MacDonald, R. Wicker, and H. Xin, "3-D printed microwave patch antenna via fused deposition method and ultrasonic wire mesh embedding technique," *IEEE Antennas Wireless Propag. Lett.*, vol. 14, pp. 1346–1349, 2015.
[31] P. Nayeri et al., "3D printed dielectric reflect arrays: Low-cost high-gain antennas at sub-millimeter waves," *IEEE Trans. Antennas Propag.*, vol. 62, no. 4, pp. 2000–2008, Apr. 2014.
[32] J. Huang, S. J. Chen, Z. Xue, W. Withayachumnankul, and C. Fumeaux, "Impact of infill pattern on 3D printed dielectric resonator antennas," in *Proc. IEEE APCAP*, 2018, pp. 233–235.
[33] Z.-X. Xia, K. W. Leung, and K. Lu, "3-D-printed wideband multi-ring dielectric resonator antenna," *IEEE Antennas Wireless Propag. Lett.*, vol. 18, no. 10, pp. 2110–2114, Oct. 2019.
[34] F. P. Chietera, R. Colella, and L. Catarinucci, "Dielectric resonators antennas potential unleashed by 3D printing technology: A practical application in the IoT framework," *Electronics*, vol. 11, no. 1, p. 64, 2022.
[35] A. Petosa, *Dielectric Resonator Antenna Handbook*. Norwood, MA, USA: Artech House, 2007.
[36] D. M. Pozar, *Microwave Engineering*. Hoboken, NJ, USA: Wiley, 2011.
[37] J. Huang, S. J. Chen, Z. Xue, W. Withayachumnankul, and C. Fumeaux, "Wideband endfire 3-D-printed dielectric antenna with designable permittivity," *IEEE Antennas Wireless Propag. Lett.*, vol. 17, no. 11, pp. 2085–2089, Nov. 2018.
[38] A. Glisson, "Electromagnetic mixing formulas and applications," *IEEE Antennas Propag. Mag.*, vol. 42, no. 3, pp. 72–73, Jun. 2000.
[39] B. Yektakhah and K. Sarabandi, "A wideband circularly polarized omnidirectional antenna based on excitation of two orthogonal circular TE21 modes," *IEEE Trans. Antennas Propag.*, vol. 65, no. 8, pp. 3877–3888, Aug. 2017.

REZA SHAMSAEE MALFAJANI (Graduate Student Member, IEEE) received the B.S. degree in electrical engineering from the University of Tehran, Tehran, Iran, in 2009, and the M.S. degree in electrical engineering from Tarbiat Modares University, Tehran, in 2012. He is currently pursuing the Ph.D. degree with Polytechnique Montréal, Montreal, QC, Canada, where he is also a member of the Poly-Grames Research Center. His research focuses on the periodic structures, antennas and RF, mm-wave, and Terahertz designs. He received the Merit Scholarship Program for Foreign Students in 2023, the Jocelyne and Jean C. Monty Doctoral Research Excellence Scholarship in 2022, and Food Agility CRC Scholarship in 2021.

HAMED NIKNAM received the Ph.D. degree from McGill University, Montreal, QC, Canada, in 2020. He is a FRQNT Award-Holder Postdoctoral Fellow with the Mechanical Engineering Department, Polytechnique Montréal. He has been a member of the Research Center for High Performance Polymer and Composite Systems since 2016. His previous research focused on 3-D printed architectured metamaterial for enhancing thermos-mechanical response of solid structures. In 2020, he has joined the Laboratory for Multiscale Mechanics, Polytechnique Montreal since. His current research are employing advanced additive manufacturing techniques for 5G applications.

SAMPADA BODKHE received the bachelor's degree in mechanical engineering from Visveswaraya Technological University, India, and the master's degree in aerospace engineering from the Indian Institute of Technology Kanpur, India, and the Ph.D. degree from Polytechnique Montréal in 2017, where she developed piezoelectric inks and a technique to co-fabricate electrodes with piezoelectric sensors via co-extrusion-based 3-D direct-write technique. She is an Assistant Professor with the Department of Mechanical Engineering, Polytechnique Montréal. The research on the development of these self-powered sensors towards aero-elastic and biomedical applications was chosen as the ten Best Discoveries of the Year 2018 by Quebec Science Magazine. As a visiting Ph.D. student with the Organic Robotics Laboratory, Cornell University, she worked on SLA based 3-D printing of highly flexible actuators. After her Ph.D., she worked as a Postdoctoral Researcher with the Composite Materials and Adaptive Systems Laboratory, ETH Zurich, on establishing competencies in 3-D printing of adaptive systems and multifunctional materials and structures. Prior to her Ph.D., she worked as an Edison Engineer with General Electric aviation, India, on structural and thermal evaluation of components for LEAP 1B engines. She has keen interests in building an additive manufacturing platform for the fabrication of intelligent composite structures. she is Currently also an Ambassador for the Montreal Chapter of Women in 3-D Printing and serves on the advisory board of Indian Women in 3-D Printing.

DANIEL THERRIAULT is a Full Professor with the Mechanical Engineering Department, Polytechnique Montreal. He currently holds the Safran-Polytechnique Industrial Chair on the additive manufacturing of reinforced polymers since 2018 and formerly held a Canada Research Chair on the fabrication of advanced microsystems and materials in 2009 to 2019. He is a Co-Director of the Laboratory for Multiscale Mechanics. Several important scientific contributions ($\sim$ 120 refereed papers) in prestigious journals, such as *Nature Materials*, *Advanced Materials*, and *Additive Manufacturing*, and multiple innovations (ten Patents), originated from the research activities of his research team. He worked or is working on many collaborative research projects with partners such as Safran Group, Bombardier Aerospace, ArianeGroup, Bell Textron Canada, 3M, Dyze Design, NanoXplore, and the Canadian Space Agency. His research interests are mainly related to additive manufacturing of advanced materials and multifunctional composites. Past contributions include the development of innovative additive manufacturing processes (e.g., freeform printing), the design and fabrication of nanocomposite materials for advanced aerospace applications and the 3-D printing of carbon fiber-reinforced thermoplastic composites.

JEAN-JACQUES LAURIN (Senior Member, IEEE) received the B.Eng. degree in engineering physics from the Ecole Polytechnique de Montreal, Montreal, QC, Canada, in 1983, and the M.A.Sc. and Ph.D. degrees in electrical engineering from the University of Toronto, Toronto, ON, Canada, in 1986 and 1991, respectively. In 1991, he joined the Poly-Grames Research Centre, Ecole Polytechnique de Montreal, where he is currently a Professor. He is the Co-director of Center for Systems, Technologies and Applications for Radiofrequency and Communications, a strategic research cluster in the province of Quebec. His research interests include antenna design and modeling, wave processing surfaces, near-field antenna measurement techniques, and electromagnetic compatibility.

MOHAMMAD S. SHARAWI (Senior Member, IEEE), is a Full Professor with the Electrical Engineering department, University of Montréal (Polytechnique Montréal), QC, Canada, where he is also a member of the Poly-Grames Research Center. He was with the King Fahd University of Petroleum and Minerals, Dhahran, Saudi Arabia, from 2009 to 2018, where he founded and directed the Antennas and Microwave Structure Design Laboratory. He was a Visiting Professor with the Intelligent Radio Laboratory, Department of Electrical Engineering, University of Calgary, Calgary, AB, Canada, in Summer-Fall of 2014 and a Visiting Research Professor with Oakland University, Rochester, MI, USA, in Summer 2013. He has more than 350 papers published in refereed journals and international conferences, 11 book chapters (two of which in the Antenna Handbook, 5th edition, McGraw Hill, 2018), one single authored book titled "*Printed MIMO Antenna Engineering*," Artech House, 2014, and the lead author of the recent book "*Design and Applications of Active Integrated Antennas*," Artech House, 2018. He has 28 issued/granted and nine pending patents in the U.S. Patent Office. His research interests include multiband printed multiple-input-multiple-output antenna systems, reconfigurable and active integrated antennas, millimeter-wave MIMO antennas and integrated 4G/5G antennas, microwave sensors, applied electromagnetics, and computational methods. He was a recipient of the Abdul Hameed Shoman Foundation Award for Arab researchers for the category of wireless systems in 2020 in addition to various best IEEE conference paper awards. He is also serving as an Associate Editor for the IEEE ANTENNAS AND WIRELESS PROPAGATION LETTERS, *IET Microwaves, Antennas and Propagation*, and *IEEE Open Journal on Antennas and Propagation*; and an Area Editor (Antennas and Microwave Devices and Systems) for *Microwave and Optical Technology Letters* (Wiley). He was the Specialty Chief Editor for the newly launched *Frontiers in Communications and Networks* journal for the System and Test-Bed design section. He has served on the Technical and organizational program committees and organized several special sessions on MIMO antenna systems and architectures in several international conferences, such as EuCAP, APS, IMWS-5G, APCAP, and iWAT. He is also the IEEE Antennas and Propagation Society Chair of the Montreal section and an Active Member of the IEEE Member benefits committee leading the initiative of the APS Student Travel grant. He is also the regional delegate of the EuRAAP in North America and a Distinguished Lecturer of the IEEE Antennas and Propagation society from 2023 to 2025.